A significant difficulty with trying to test a complex three-dimensional trajectory is the ability of the pilot to follow the computed state and control variables. In two dimensions, this can be accomplished, particularly after some practice in a simulator.[2] This increases the importance of considering the use of an autopilot for flying the trajectory and thus reducing the pilot workload. Currently, optimal trajectories are computed in a desktop computer, usually requiring a skilled operator to solve a given problem. To reach the goal of using an autopilot for following the optimal trajectory, the numerical method needs significant improvement in two areas.

First, although microprocessors, such as the Intel Pentium II/III, quickly become more powerful, it is still not quite possible to solve a problem in real time. Currently, the numerical implementation used in this Note runs on a 400 MHz Pentium laptop running the Linux operating system. At best, a given problem of 500–1000 variables can be solved in 15–20 s. This type of performance is achieved by solving the problem on several discretization grids, starting with a coarse grid and then by using this solution as initial approximation on the finer grids. To significantly improve this performance, it is necessary to use a second-order method with exact second derivatives instead of the quasi-Newton method[9] used here.

Another issue that needs to be resolved concerns the robustness of the solution method. It is in principle impossible to a priori estimate how many iterations are needed to solve a nonlinear problem. Small changes to a given problem may drastically increase the amount of computing necessary to solve the problem. As a first step toward finding the optimal trajectory in real time, one can attempt to update a precomputed trajectory when initial and final conditions are perturbed. This way it may become possible to follow a moving target and also adjust for minor inaccuracies in performance modeling and atmospheric data. In principle this means that the solution of the nonlinear optimization problem approaches a closed-loop control method, as opposed to the open-loop approach used today.

Acknowledgments

This project is financially supported by the Swedish Defense Materiel Administration (FMV) project 61969-LB104302. The author is most grateful for the support provided by the staff of FMV: KCFlyg, in particular Martin Näsman. The author is also most grateful for the support of Philip Gill at University of California at San Diego and Walter Murray and Michael Saunders at Stanford University.

References

[1]Hargraves, C. R., and Paris, S. W., "Direct Trajectory Optimization Using Nonlinear Programming and Collocation," *Journal of Guidance, Control, and Dynamics*, Vol. 10, No. 4, 1987, pp. 338–342.

[2]Ringertz, U. T., "Flight Testing an Optimal Trajectory for the Saab J35 Draken," *Journal of Aircraft*, Vol. 37, No. 1, 2000, pp. 187–189.

[3]Etkin, B., and Reid, L. D., *Dynamics of Flight, Stability and Control*, Wiley, New York, 1996.

[4]Brenan, K. E., "Differential-Algebraic Equations Issues in the Direct Transcription of Path Constrained Optimal Control Problems," The Aerospace Corp., Aerospace Rept. ATR-94(8489)-1, 1993.

[5]Ringertz, U. T., "Multistage Trajectory Optimization Using Large-Scale Nonlinear Programming," TR 99-25, Royal Inst. of Technology, Dept. of Aeronautics, 1999.

[6]Pouvreau, L., "Re-Engineering of Combat Aircraft: Lockheed-Martin F-16C," Daimler-Benz Aerospace, ECATA-Junior Multinational Team Project, 1997.

[7]Webb, T. S., Kent, D. R., and Webb, J. B., "Correlation of F-16 Aerodynamics and Performance Predictions with Early Flight Test Results," *AGARD Conference Proceedings CP-242*, Advisory Group for Aerospace Research and Development, Neuilly sur Seine, France, 1978.

[8]Vinh, N., *Flight Mechanics of High-Performance Aircraft*, Cambridge Aerospace Series 4. Cambridge Univ. Press, Cambridge, England, U.K., 1993.

[9]Gill, P. E., Murray, W., and Saunders, M. A., User's Guide for SNOPT 5.3: A FORTRAN Package for Large-Scale Nonlinear Programming, Rept. NA 97-X, Dept. of Mathematics, Univ. of California, San Diego, CA, 1997.

Computational Analysis of F-15 Forebody Flow at High Alpha

Kenneth E. Wurtzler*
U.S. Air Force Research Laboratory, Wright–Patterson Air Force Base, Ohio 45433-7913

Introduction

WITH flight envelopes being expanded because of changing tactics and engineering ability, fighter aircraft are designed and expected to fly at higher angles of attack and maintain directional control. However, the vertical tails become surrounded by turbulent, dead air and are limited in their directional control capability at high angles of attack. Relatively small side forces on the nose, even at zero sideslip, can dominate directional stability and create large yawing moments. These small side forces are a result of asymmetrical shedding of the forebody vortices. Small surface imperfections such as radome gaps, dents, and sharp paint depth mismatches can affect the strength and path of the vortices. The resultant net yawing moment can then increase, and the aircraft becomes unstable—an unsteady phenomenon that can be catastrophic.

In this study the F-15 forebody with varying tip geometries was modeled to match the geometry from a wind-tunnel test.[1] The three geometries were bump, bump with strakes, and bump with tabs. The length of the full-scale forebody section was 13.4 ft with the aft end being blunt. The grid-generation package VGRIDns[2] was used to generate an unstructured tetrahedral grid. The bump grid consists of 1.6 millions cells with the bump modeled on the lower left quadrant of the forebody, near the apex, by creating a small ridge of 0.3 in. maximum height on the surface. The bump with strakes grid contains 2.4 million cells with the strakes modeled as thin wedges. Each strake was 10 in. long and 1 in. wide. The bump with tabs grid consists of 1.8 million cells. The tabs consist of the first inch of the strakes. Cells are clustered near the strakes and tabs. Far-field boundaries for all grids are 10 forebody lengths away.

Cobalt_{60} (Ref. 2) is a parallel, implicit unstructured flow solver, which employs Godunov's first-order accurate, exact Riemann method. Second-order spatial accuracy, second-order accurate implicit time stepping, viscous terms, and turbulence models have been added to this procedure. Cobalt_{60} uses a finite volume, cell-centered approach. Arbitrary cell types can be used, and a single grid can be composed of a variety of cell types. The implicit algorithm in Cobalt_{60} was implemented and demonstrated by Tomaro et al.[3] in 1997. The development of the parallel version of Cobalt_{60} was reported by Grismer et al.[4] Domain decomposition is the basis for the parallel code with each processor operating on a subsection (zone) of the original grid.

Results and Discussion

Flow conditions are the same as wind-tunnel test conditions.[1] The dynamic pressure was 10 psf, the corresponding flow velocity was 92 ft/s, and the Reynolds number nearly 5×10^4/in. Flow was assumed to be laminar. For most of the runs, 48 nodes were used, which gave a timing of 13.2 μs/cell/iteration. Several runs utilizing 140 nodes took 4.2 μs/cell/iteration. For a 2-million cell grid this amounts to 26.2 s/iteration for 48 nodes and 8.4 s/iteration for 140 nodes. All force and moment data presented in this Note are in body-axis system and are resolved at the F-15's aerodynamic

Received 31 January 1999; revision received 22 October 1999; accepted for publication 31 October 1999.

*Aerospace Engineer, Computational Sciences Branch, Air Vehicles Directorate.

reference point at FS 557.173, WL 116.173, and BL 0. All aerodynamic coefficients are calculated based on the standard F-15 dimensions with $S = 608$ ft^2, MAC $= 15.94$ ft, and $b = 42.8$ ft. The force and moment data that were acquired used only the first 12 ft of the F-15 forebody. The test data were gathered from 256 pressure ports on the forebody (8 rows of 32 ports). These test data were then smoothed and transformed into the visual results for selected cases. The view of all of the surface plots is looking *at* the forebody. The definitions of right and left are from the *pilot's* point of view.

The purpose of the bump validation is to determine the adequacy of the asymmetric geometry in the computational analysis to reproduce the experimental asymmetry. The first comparison of static yawing moment is shown in Table 1 for 0 deg β. At 40 deg α both the computational and experimental data show a negative yawing moment. At 62 deg α the yawing moment increases in magnitude in both cases by the same amount. The addition of the 10-in. strakes in both cases reduces the yawing moment substantially at both angles of attack.

The test data available for comparison consists of plots of surface *Cp* on the bump forebody with and without strakes. At 62 deg α and 0 deg β the influence of the bump can be seen in both the computational and experimental data (Fig. 1). The stagnation region is evident on the underside centerline. As the flow accelerates around the forebody, low-pressure regions are created. The bump side low-pressure region is reduced because of its presence. As the flow reaches the adverse pressure gradient on the top half of the forebody, it separates into a pair of off-body vortices. This is exhibited in the prong-like features emanating from the tip. The shedding vortex is altered in its growth and its direction on the bump side. The yawing moment is negative because of the larger suction region on the windward side (Table 1), creating a nose right force. When the strakes are added to this geometry (Fig. 2), the flow is returned to more symmetrical behavior, and the yawing moment is lessened considerably as seen in Table 1. Additionally, flow symmetry is increased by the dominating vortices at the apex of the forebody, which shows the importance of that region in yaw control.

The addition of control devices on the forebody is aimed at reducing the large, adverse yawing moments caused by geometric imperfections near the forebody tip. The bump case produces a nose right yawing moment at all sideslip angles, with the largest moment at -10 deg β and decreasing down to 20 deg β (Fig. 3). The 10-in. strakes improve the directional characteristics at 62 deg α by decreasing the magnitude of the yawing moment caused by the bump case. The tabs produced mixed results throughout the beta sweep. At beta angles between -10 deg and 0 deg β, the tabs exhibit a favorable trend that dissolves at positive β. It is possible that the tabs are too small in comparison to the bump for their influence to dominate at higher beta angles.

A flowfield analysis of streamlines and pressure isosurfaces for 20 deg β and 62 deg α is shown in Figs. 4 and 5. The suction on

Table 1 Comparison of experimental and computational yawing moments at 0 deg β

α, deg	Bump EXP	Bump CFD[a]	Strake EXP	Strake CFD
40	−0.00068	−0.00077	−0.00039	−0.00032
62	−0.0141	−0.0126	−0.007	−0.0062

[a]Computational fluid dynamics.

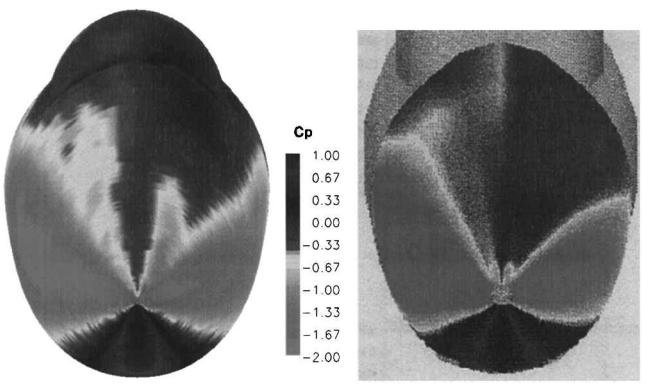

Fig. 1 Plot of surface *Cp* with computational (left) and experimental (right) data on forebody with bump. α = 62 deg and β = 0 deg.

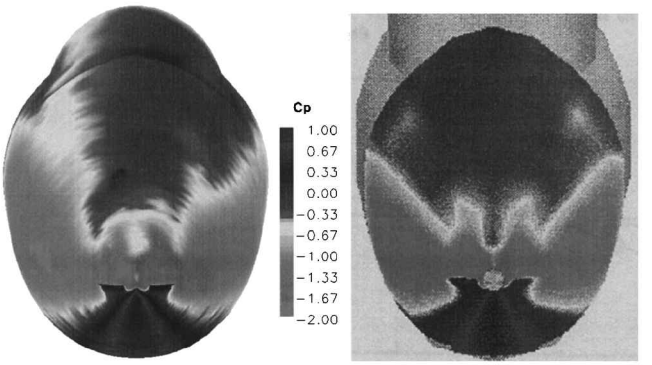

Fig. 2 Plot of surface *Cp* with computational (left) and experimental (right) data on forebody with bump and 10-in. strakes. α = 62 deg and β = 0 deg.

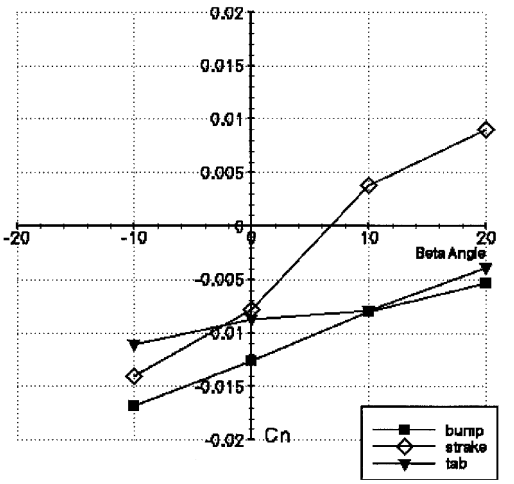

Fig. 3 Effect of 10-in. strakes and tabs on directional characteristics. α = 62 deg.

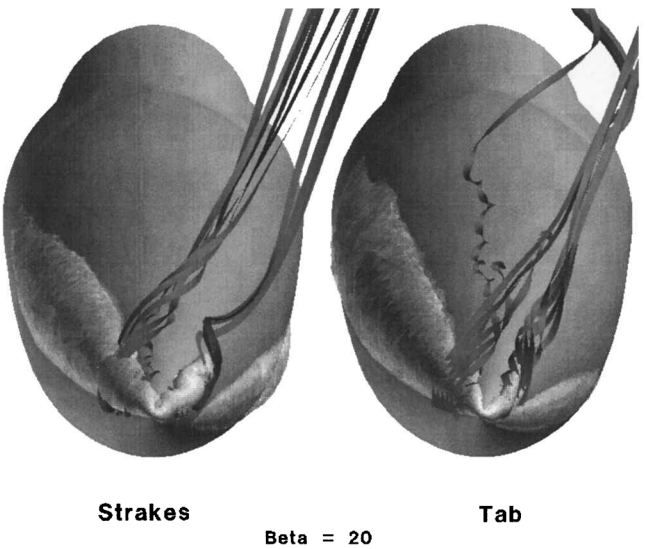

Fig. 4 Isosurface of pressure with streamlines off control devices. α = 62 deg and β = 20 deg.

creasing the magnitude of the yawing moment caused by the bump case. The tabs produced mixed results throughout the beta sweep. At beta angles between -10 deg and 0 deg β, the tabs exhibit a favorable trend that dissolves at positive β. It is possible that the tabs are too small in comparison to the bump for their influence to dominate at higher beta angles.

A flowfield analysis of streamlines and pressure isosurfaces for 20 deg β and 62 deg α is shown in Figs. 4 and 5. The suction on

Fig. 5 Oil flow for α = 62 deg and β = 20-deg case.

the windward side is larger in the tab case, whereas the strakes act more to even out the regions. Plus, the high-energy vortices from the strakes provide a stabilizing influence over the bump asymmetry. This allows the effect of the sideslip angle, not the physical imperfection, to control the yawing moment.

The effect of these control devices on the static pitching moment has to be considered along with their impact on lateral directional stability. At sideslip angles any increase in nose-up effect can be detrimental. The strake does an extraordinary job of limiting an increase in C_m (Table 2). When compared to the bump case, C_m is lower for each angle-of-attack case. The addition of the control devices limits the vertical growth of the suction region on the sides of the forebody.

Table 2 Effectiveness of two forebody control devices on pitching moment

β, deg	Bump	Strakes	Tab
−10	0.0467	0.0472	0.0470
0	0.0569	0.0554	0.0527
10	0.0624	0.0557	0.0601
20	0.0837	0.0536	0.0679

References

[1] Kay, J., Kloc, S., and Stowe, E., "High Angle of Attack Full-Scale F-15 Forebody Wind Tunnel Testing," Bihrle Applied Research, Inc., BAR 97-4, June 1997.

[2] Strang, W. Z., Tomaro, R. F., and Grismer, M. J., "The Defining Methods of Cobalt$_{60}$: A Parallel Implicit, Unstructured Euler/Navier–Stokes Flow Solver," AIAA Paper 99-0786, Jan. 1999.

[3] Tomaro, R. F., Strang, W. Z., and Sankar, L. N., "An Implicit Algorithm for Solving Time Dependent Flows on Unstructured Grids," AIAA Paper 97-0333, Jan. 1997.

[4] Grismer, M. J., Strang, W. Z., Tomaro, R. F., and Witzeman, F. C., "Cobalt$_{60}$: A Parallel, Implicit, Unstructured Euler/Navier–Stokes Solver," *Advances in Engineering Software*, Vol. 29, No. 3–6, 1998, pp. 365–373.